Faraday Discussions

Cite this: *Faraday Discuss.*, 2014, **176**, 95

PAPER

In situ TEM study of the Li–Au reaction in an electrochemical liquid cell

Zhiyuan Zeng,[a] Wen-I. Liang,[ab] Ying-Hao Chu[b] and Haimei Zheng*[ac]

Received 1st July 2014, Accepted 24th July 2014
DOI: 10.1039/c4fd00145a

We study the lithiation of a Au electrode in an electrochemical liquid cell using transmission electron microscopy (TEM). The commercial liquid electrolyte for lithium ion batteries (1 M lithium hexafluorophosphate $LiPF_6$ dissolved in 1 : 1 (v/v) ethylene carbonate (EC) and diethyl carbonate (DEC)) was used. Three distinct types of morphology change during the reaction, including gradual dissolution, explosive reaction and local expansion/shrinkage, are observed. It is expected that significant stress is generated from lattice expansion during lithium–gold alloy formation. There is vigorous bubble formation from electrolyte decomposition, likely due to the catalytic effect of Au, while the bubble generation is less severe with titanium electrodes. There is an increase of current in response to electron beam irradiation, and electron beam effects on the observed electrochemical reaction are discussed.

Introduction

In commercial lithium-ion batteries, the most commonly used anode materials are graphitic carbon or other carbonaceous materials, since such materials are cheap, have good cyclability and the working voltage is low.[1,2] However, the theoretical capacity of a carbon electrode is only 372 mA h g^{-1}. To decrease the reduction of the cell voltage and thereby increase the energy density, anode materials with extremely negative potentials and high capacities have been investigated. Metals or other materials including Sn, Cu, Sb and Si that can be alloyed with lithium are promising candidates due to their high theoretical capacities.[3–10] Gold (Au) reacts with lithium at low voltage forming several lithium–gold alloy phases, including ones with a very high percentage of Li (up to Au_4Li_{15}).[11] A Au electrode can be used as the anode (although it is not cost effective) since it has a wide range of stable cell voltages and the lowest possible alloying/de-alloying potential relative to the Li/Li^+ couple. It is known that any deviation from the potential of the Li/Li^+ couple will be at the expense of the

[a]*Materials Sciences Division, Lawrence Berkeley National Laboratory, Berkeley, CA 94720, USA. E-mail: hmzheng@lbl.gov*
[b]*Department of Materials Science and Engineering, National Chiao Tung University, Hsinchu, 30010, Taiwan*
[c]*Department of Materials Science and Engineering, University of California, Berkeley, California 94720, USA*

overall cell voltage, and the net effect will be a reduction in the energy density of the battery. The major problem encountered in gold, as well as other materials, is the large volume change due to structural changes accompanying lithiation and delithiation. The mechanical stress generated during these lithium uptake and release processes will cause pulverization and quick capacity fading,[7] which makes these materials not very practical for long term usage. Current strategies to overcome the pulverization of electrodes mainly focus on a reduction of the particle size, the use of composite materials, and optimization of the binder material. However, the reaction mechanisms of these materials with lithium are still far from being completely understood.

In situ liquid cell TEM allows the imaging of chemical reactions in liquids with high spatial resolution,[12–19] which provides the opportunity to address important questions regarding the electrode–electrolyte interfaces in a battery cell. We study the Au electrode reaction with lithium during charging and discharging using an electrochemical liquid cell under a transmission electron microscope. In previous reports using gold as an anode material for lithium ion batteries, although both *ex situ* and *in situ* studies were applied and different Au–Li alloy phases have been achieved,[4,11,20–22] the Au–Li reaction has never been observed directly. Recently, utilizing our newly designed electrochemical liquid TEM cells, we have captured the dynamic processes of inhomogeneous lithiation, lithium metal dendritic growth, electrolyte decomposition and solid–electrolyte interface formation.[23] Here, using the same electrochemical liquid cell, we captured different types of lithiation reaction for a Au electrode in a commercial battery electrolyte by real time imaging. The catalytic role of Au in electrolyte decomposition and beam effects are discussed based on control experiments or theoretical calculations.

Experimental

The electrochemical cells were fabricated following a procedure similar to that reported previously.[23] We used ultra-thin silicon wafers (200 μm, 4 inches, p-doped) purchased from Virginia Semiconductor (Fredericksburg, VA). A 25 nm thick low stress silicon nitride film was evaporated on the silicon wafer as a membrane of the viewing window. The viewing windows and two reservoirs were created by photolithographic patterning and etching with KOH solution (with water to KOH ratio of 2 : 1). The dimensions of the windows were 25 μm × 6 μm. Two 120 nm-thick gold electrodes were deposited on the bottom chips with a face-to-face distance of 20 μm. The bottom and top chips were bonded together with a 150 nm thick sputtered indium spacer. The commercial electrolyte for lithium ion batteries, *i.e.* 1 M lithium hexafluorophosphate $LiPF_6$ dissolved in 1 : 1 (v/v) ethylene carbonate (EC) and diethyl carbonate (DEC), was loaded into one of the reservoirs with a syringe. We sealed the cell, including the reservoirs, using Cu foil and epoxy. Since the window gap is less than 150 nm, no contamination from the epoxy was observed during the electrochemical experiments. The dimensions of the biasing cell were ~3 mm × 3 mm in a square and ~400 μm thick. Both of the working and counter electrodes were extended to two gold pads in two reservoirs. Gold wires were bonded onto each gold pad and they were connected to the two copper pads on the TEM holder tip, which allow an electric bias to be applied. The cells were fabricated at the Marvell Nanofabrication Laboratory of the University of California at Berkeley. The TEM holder fits a JEOL 2100 TEM operated at 200 kV.

Real-time videos of the electrochemical experiments were recorded at 2–15 frames per second. Faster recording, up to 400 frames per second, was also incorporated using a high speed camera provided by Direct Electron, LP (San Diego, CA) with a model number DE-12. The electrochemical process was controlled by an electrochemical workstation (Model 660D series made by CH Instruments) connected to the TEM holder. It was used to perform *in situ* cyclic voltammetry measurements.

For *ex situ* experiments, we first put a droplet of Au nanowire solution (used as purchased from Nanopartz Inc.) onto the lacey carbon Cu grids and let the Cu grids dry out so that lots of Au nanowires were attached to the carbon film. Then, the TEM grids were immersed into the lithium electrolyte with a short face-to-face distance. The two Cu grids were connected to an electrochemical working station and cyclic voltammetry with a voltage range of 0 to −3 V and a scan rate of 0.1 V s^{-1} was applied. The morphology changes and lithiated alloy phases were examined in great detail under TEM as a comparison to the *in situ* results.

Results and discussion

A scheme of how the gold electrode reacts with the lithium ion battery electrolyte in the electrochemical liquid cell set up is shown in Fig. 1. The bottom left of Fig. 1 shows a real electrochemical liquid cell with Au wires bonded onto the Au pads on the bottom chip in the reservoir area. In the home-made TEM holder, a cell pocket is designed to fit and hold the electrochemical liquid cell. Currently, only two electrodes are used. In the future, a reference electrode can be added. When the electrolyte $LiPF_6$/EC/DEC was loaded into one of the two reservoirs, the electrolyte flowed into the cell by capillary force and a thin liquid layer (~120 nm) was formed at the observatory window and everywhere inside the cell. We applied cyclic voltammetry and monitored the electrode–electrolyte interface under TEM. The dynamic reaction of the Au electrode with Li was captured in real time.

The phase diagram of the Au–Li binary system is shown in Fig. 2.[24] The alloys of Au_5Li_4, AuLi, $AuLi_3$ and Au_4Li_{15} are expected to form during the lithiation of

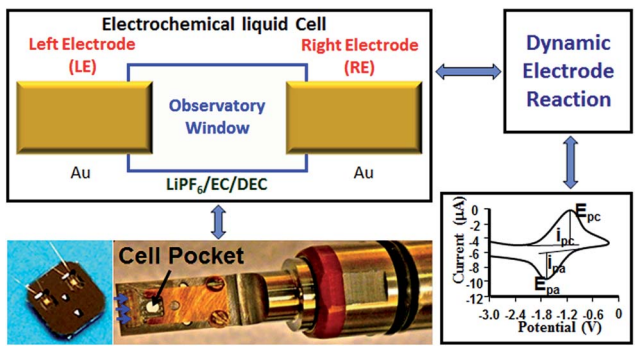

Fig. 1 A scheme of the *in situ* TEM set up for the observation of the electrochemical reaction using an electrochemical liquid cell. 120 nm thick gold (or Ti) electrodes are used. The dynamic electrochemical reaction on the electrode corresponding to the applied cyclic voltammetry is captured. The bottom left photographs show an electrochemical liquid cell and a home-made TEM holder.

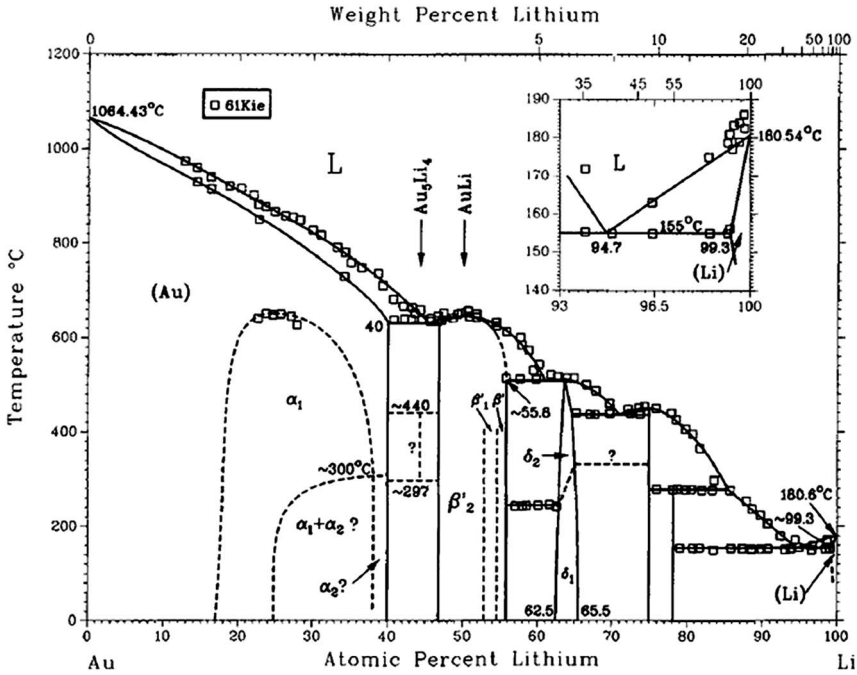

Fig. 2 Au–Li phase diagram.[24] With kind permission from Springer Science and Business Media.

gold at equilibrium conditions. However, these crystalline (Li, Au) compounds may not form directly during the electrochemical-driven alloying of Au with Li, despite the fact that the formation energies of the crystalline (Li, Au) compounds are lower than those of the corresponding amorphous phases, similar to the lithiation reaction of Si.[25] A recent study of lithium alloying with a gold electrode, conducted by *in situ* XRD, revealed that during the electrochemical cycling of the gold electrode two different crystalline Au–Li alloy phases were observed. For instance, $AuLi_1$ was formed during charging of the gold electrode. During discharging, $AuLi_1$ converted into $AuLi_2$ and subsequently dissolved, leaving an amorphous phase. Both the $AuLi_1$ and $AuLi_2$ phases are not shown in the Au–Li phase diagram, which suggests that they are metastable.[22] We aim to image in detail the phases and phase transitions accompanying the morphology changes during the Au–Li reaction. Here, we report the morphology changes and reaction kinetics during lithiation of the gold electrode from *in situ* observation. From our *ex situ* studies, only the Au_3Li phase was achieved, which is reasonable since only stable phases are expected after the reaction. A detailed *in situ* study of the phases and phase transitions during the reaction is in progress and the results will be reported in a future publication.

Fig. 3A–I show sequential images of the electrolyte decomposition, lithiation of the gold electrode and subsequent dissolution of the gold electrode during a discharge–charge cycle at an early stage. At the beginning, a sharp interface between the Au electrode and $LiPF_6$/EC/DEC is observed indicating that no reaction occurred. When the cyclic voltammetry is ramped down to

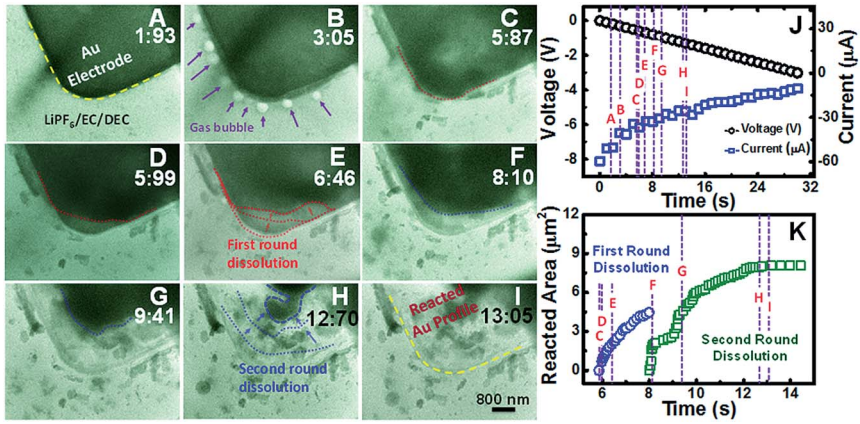

Fig. 3 (A)–(I) Time evolution of the dissolution of the Au electrode in the $LiPF_6$/EC/DEC electrolyte; (J) the corresponding applied electric potential and measured electric current from frame A to frame I; (K) the evolution of the dissolved area of the Au electrode as a function of time during cyclic voltammetry with the voltage range of 0 to −3 V and a scan rate of 0.1 V s^{-1}.

−0.3 V, many bubbles are formed, which suggests gaseous products are generated from electrolyte decomposition.[23] In the meantime, a thin Li–Au layer is formed because of the interfacial reaction between the Au electrode and the lithium ion battery electrolyte. Subsequently, the Au electrode reacts vigorously with the electrolyte, resulting in the Au layer stripping and dissolving from the outer layer to the inner part of the electrode. The starting etching point is the corner of the Au electrode, then the reaction front propagates along the diagonal direction (Fig. 3C–E). A large part of the Au corner is etched away within 2 s, defined as the "first round dissolution". The contrast changes from dark to light due to the surface layer of the Au electrode reacting and dissolving in the electrolyte. After the surface layer is peeled off, the exposed new surface area of the Au electrode reacts with the electrolyte resulting in "second round dissolution". As shown in Fig. 3F–H, the reaction front moves promptly in a diagonal direction from 8.10 s to 12.70 s, and almost all the Au electrode vanishes. Fig. 3J shows the corresponding applied electrical potential and the measured electrical current from frames (A)–(I), where the applied voltage is ramping from 0 V to −3 V and the measured electrical current decreases. It is noted that the measured electric current under TEM is higher than that from the same electrochemical liquid cell without an electron beam, and beam effects will be discussed in a later section. The reaction kinetics are measured by the dissolution area of the Au electrode as a function of time (Fig. 3K). In the first round dissolution, an area of 4.5 μm^2 is etched away within 2 s under −0.6 V to −0.8 V, thus the etching speed of the Au electrode is 2.25 μm^2 s^{-1}. The Au etching speed of the second round dissolution in the voltage range of −0.8 V to −1.4 V is 1.33 μm^2 s^{-1}. Intensive Au dissolution mostly occurs in the voltage range of −0.6 V to −1.4 V. According to Bach *et al.*,[22] metastable $AuLi_2$ can be formed and then dissolved during cyclic voltammetry. We captured the signal of dissolved gold in the area surrounding the electrode (Fig. 5).

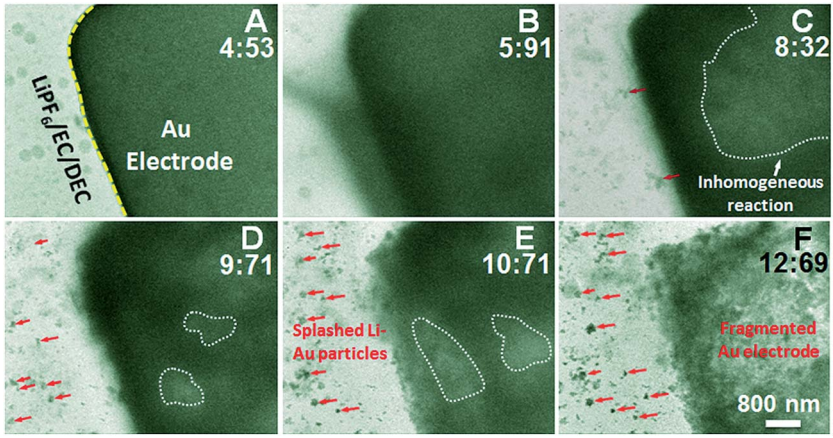

Fig. 4 Time series of TEM images showing the inhomogeneous reaction and fragmentation of the Au electrode during the Li–Au reaction. During this explosive reaction, a large number of nanoparticles splash from the Au electrode to the area surrounding the electrode.

Another type of Li–Au reaction that was observed is the explosive reaction of the Au electrode. In this case, during lithiation of the Au electrode, electrolyte decomposition is still expected but no gaseous products (bubbles) are released. It is likely that the gaseous products are absorbed and accumulated on the surface of the electrode, which triggers the explosion of the Au electrode at a later stage. This explosion generates a large number of Au or Li–Au nanoparticles, since Au or

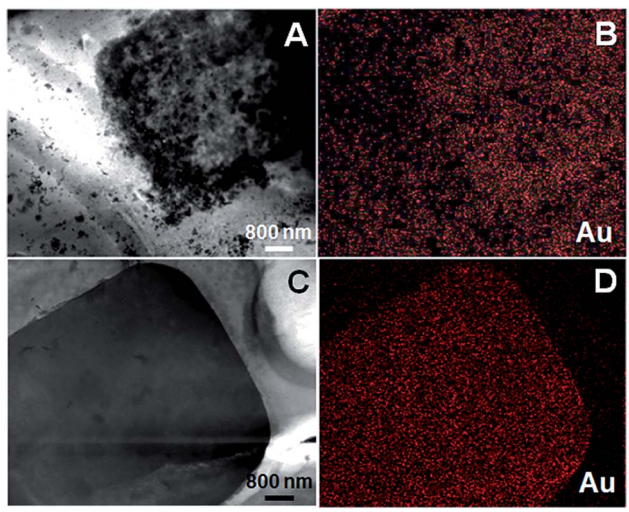

Fig. 5 (A) HAADF image of the right Au electrode that was electrochemically reacted with the lithium electrolyte (also shown in Fig. 4F). (B) The corresponding EDS map of (A). (C) The left side of the Au electrode. (D) The corresponding EDS map of the Au electrode in (C).

lithiated Au can peel off from the Au electrode during the explosion. In Fig. 4A–F, the sequential images show such an explosive Au lithiation reaction. Initially, the Au electrode is intact with a clean, sharp interface with the electrolyte. When the cyclic voltammetry is ramped down in the negative direction, an inhomogeneous reaction occurs as marked with a white dash line in Fig. 4C. Subsequently, the splashing of nanoparticles accompanied by erosion of the electrode takes place. The number of splashed particles dramatically increases within 3 s, and they reside in the area surrounding the fragmented electrode.

We performed energy dispersive X-ray spectroscopy (EDS) mapping of the reacted Au electrode, with the fragmented Au electrode and many small nanoparticles in the surrounding area, as well as the other side of the electrode. Fig. 5B and D show the elemental distribution profiles of Au in both the reacted and unreacted electrodes. In the reacted Au electrode residual, there is a higher concentration of Au at the edge than the inner part, indicating an inhomogeneous Li–Au reaction. The front area of the Au electrode has a higher intensity of Au, which corresponds to a stronger electric field during the reaction. It is clear that the particles splashed from the electrode during Au lithiation contribute to the measured Au signal in the EDS map. It also shows that there is Au in the "clean" area between the particles, suggesting a fraction of Au is dissolved in the electrolyte. On the other side of the Au electrode, we observe a sharp edge with Au uniformly distributed across the electrode.

In addition to the two types of reactions above, expansion and shrinkage of the Au electrode during discharging and charging are observed. This type of reaction is classical and frequently reported in the literature,[20] which is probably because such a reaction can easily be confirmed by *ex situ* characterization techniques, although detailed reaction dynamics are lacking. The sequential images in Fig. 6A–F show the morphology changes of the Au electrode during lithiation and delithiation. When the voltage is ramped down to −1.7 V, electrolyte bubbles start to form (Fig. 6A). This is followed by an expansion in the front part of the Au electrode (Fig. 6B), indicating that the Au is lithiated. The intensive expansion of

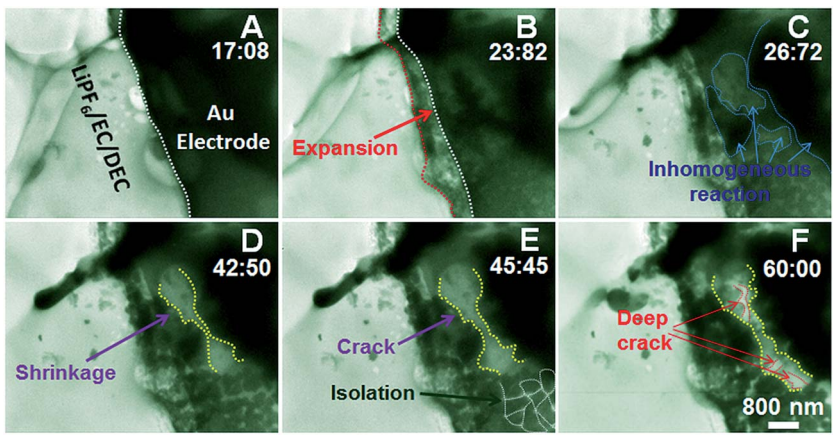

Fig. 6 Evolution of the Au electrode when electrochemically reacted with the lithium electrolyte. Expansion, cracking and partial shrinkage are observed.

the electrode induces cracks. The inhomogeneous reaction becomes more and more obvious and some heavy lithiated regions are distributed in the Au electrode. The electrode area with darker contrast represents light lithiation, while the brighter contrast indicates heavy lithiation, as marked by the blue dash line in Fig. 6C. During the charging process, shrinkage of the electrode is observed as indicated by the contour changes of the lithiated regions.

Au is likely catalyzing the electrolyte decomposition during the charge cycles. We saw lots of bubbles in Fig. 3 in the voltage range of 0 to −3 V. There are several factors influencing the electrolyte decomposition, including the applied voltage and irradiation by the electron beam. Our control experiments suggest the generation of gas bubbles is primarily due to electrolysis of the electrolyte. In a previous paper,[23] we discussed that the beam effect is secondary to electrolysis in electrolyte decomposition, since there is no bubble formation without an electric bias. Here, we found that Au may catalyze the electrolysis of the electrolyte. This is not surprising since Au is catalytically active in many chemical reactions,[26–29] including those in CO oxidation, Li–O_2 batteries and so forth. Fig. 7A–C (as well as Fig. 3) show that the Au electrode is clear with no reactions at the beginning (Fig. 7A). When the voltage is ramped down in the negative direction, many bubbles appear on the front of the electrode. Small bubbles can accumulate and merge into larger ones of up to several micrometers, as highlighted in Fig. 7B and C. At room temperature, an equilibrium exists:[23,30]

$$LiPF_6\ (s) \leftrightarrow LiF\ (s) + PF_5\ (g) \quad (1)$$

In the presence of non-aqueous solvents, PF_5 tends to cause the decomposition of carbonates:[30]

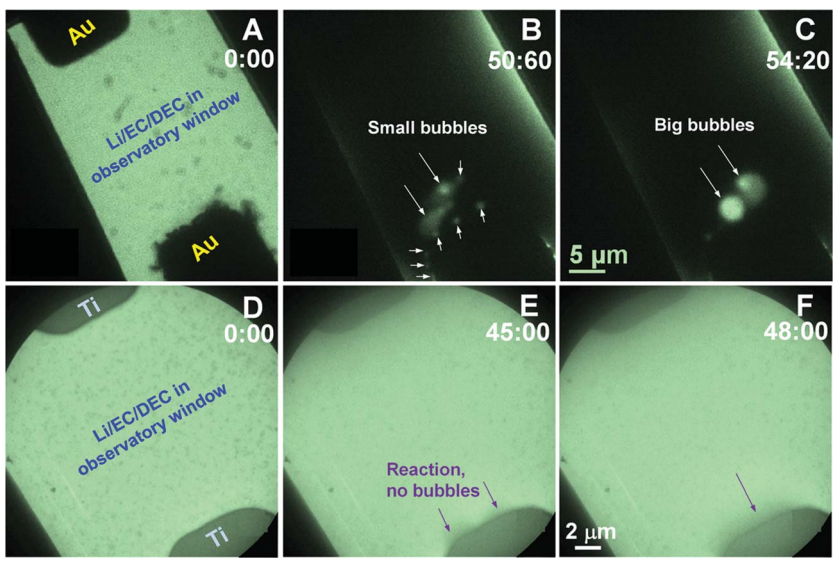

Fig. 7 Sequential images show the electrode–electrolyte interface reaction on both sides of the electrodes in two electrochemical cells. Au electrodes are used in (A)–(C) and Ti electrodes are used in (D)–(F).

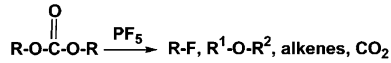

(2)

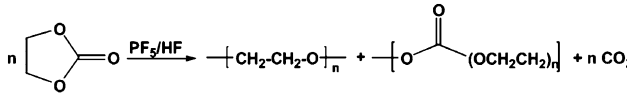

(3)

It is also known that moisture can induce the hydrolysis of $LiPF_6$ salts:[30]

$$LiPF_6\ (sol.) + H_2O \leftrightarrow LiF\ (s) + 2HF\ (sol.) + POF_3\ (sol.) \quad (4)$$

$$PF_5\ (sol.) + H_2O \leftrightarrow 2HF\ (sol.) + POF_3\ (sol.) \quad (5)$$

In our experiments, we loaded the electrolyte in a glove-box so that the moisture effects were minimized. It is likely that Au is catalyzing the above reactions 1–3. For our control experiments, we used Ti electrodes to replace the Au electrodes. The results show that, when cyclic voltammetry is applied in the voltage range of 0 to −3 V, no severe bubble formation is observed (Fig. 7E and F). This supports Au catalyzed bubble formation from electrolyte decomposition.

The electron beam has a strong effect on the current measured from the electrochemical liquid cell under TEM. Previously, we have shown that there is a drastic increase of the current when the cell is exposed to the electron beam.[31] Here, we show the cyclic voltammetry curves measured in an electrochemical cell with/without the electron beam. Fig. 8A is the CV curve without the electron beam passing through. It shows that when the voltage is ramped down from 0 to −3 V, there is a reduction peak located at −2.1 V, corresponding to the lithiation reaction of the Au electrode. When the voltage is swept back from −3 V to 0 V, there is an oxidation peak located at −1.45 V, which is attributed to the delithiation reaction of the Au electrode. It is noted that the reduction and oxidation peaks of −2.1 V and −1.45 V are not the exact lithiation/delithiation voltages of Au electrodes in lithium ion batteries, since there is no lithium reference electrode in the set up. However, it is clear that the CV plot without the electron beam show

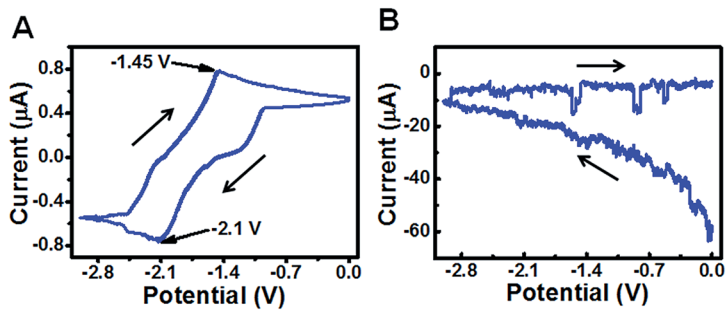

Fig. 8 Cyclic voltammetry without (A) or with (B) the electron beam passing through the SiN_x membrane in the same electrochemical liquid cell.

reduction/oxidation peaks corresponding to lithiation/delithiation of the Au electrode. When the electron beam passes through the electrochemical liquid cell, the CV plot changes drastically with strong current increases (Fig. 8B). As the voltage ramps from 0 to −3 V, the current decreases from −63 to −10 μA. Then, when the voltage is swept back to the positive direction, the current maintains a steady state in the −4 to −6 μA range, where the peak current without the electron beam is only 0.77 μA. By comparing these two CV curves, we conclude that in the current experiments, the major component of the measured current is from the electron beam.

The current changes due to the electron beam can be calculated based on the TEM imaging conditions and the electrochemical cell set up. We used an electron current density (J) of 2.5×10^3 electrons $Å^{-2}$ s^{-1} during imaging and the area (S) of the Au electrode exposed to the electron beam is $S = 2Lw$, where L is the length ($L = 10$ μm) and w is the width ($w = 6$ μm) of the Au electrode exposed to the electron beam. The current is measured in Amps (charge per second) and 1 A = -6.241×10^{18} e s^{-1}, therefore, the current (I) generated from the electron beam can be calculated: $I = JS = 2JLw = -5$ μA. The calculated value is comparable with the current measured by the electrochemical working station under the cyclic voltammetry program. This further confirms that the current increase is due to electrons collected directly by the electrodes from the electron beam. How such electrons affect the electrochemical reaction, including electrolyte decomposition, needs to be further studied. The thickness of the Au electrode in the current electrochemical liquid cells is about 120 nm. We expect that when the thickness of the electrode is reduced, the current increase from electron beam irradiation can be reduced.

Although the morphology changes of the Au electrode during the reaction with Li have been observed in great detail as discussed above, it is a great challenge to characterize the structure of the intermediate Li–Au alloy phases, due to the fast reaction kinetics and the amorphous-like reaction products dissolving at the end. We did parallel *ex situ* experiments to show the composition and crystal structure of the lithiated Au. As shown in Fig. 9,[23] when a single crystal Au nanowire is lithiated, both the morphology and crystal structure are changed. The electron diffraction pattern confirms the FCC structure of the Au crystal (space group $Fm\bar{3}m$) (inset of Fig. 9A). After cyclic voltammetry, the initially straight Au nanowire becomes twisted with a meandering morphology (Fig. 9B). Using selected area electron diffraction, we further identified the phases of the Li–Au section. The $Li_{15}Au_4$ phase is marked by the red circles (inset of Fig. 9B).[20] The blues circles are attributed to the original cubic structure of Au (space group $Fm\bar{3}m$). The atomic resolution of Au and Li ordering in an electrochemically treated Au nanowire reveals a L12 (Au_3Li) Li–Au structure in co-existence with the pure Au lattice (111) lattice planes[4,32] (Fig. 9C). From spatially resolved electron energy loss spectroscopy (EELS) spectra (Fig. 9D and E), the Au core with a Li–Au alloy shell can be achieved. The Li concentration profile can be extracted by integrating the near edge signal from 56–65 eV, as shown in Fig. 9E. The Au concentration is almost the same with no obvious deviation along the red dash line of the cross section of the Au nanowire. However, the Li concentration is lower in the center of the Au wire, indicating that the electrochemical lithiation starts from the surface of the Au wire, and Li propagates and diffuses towards the core.[23] Such *ex situ*

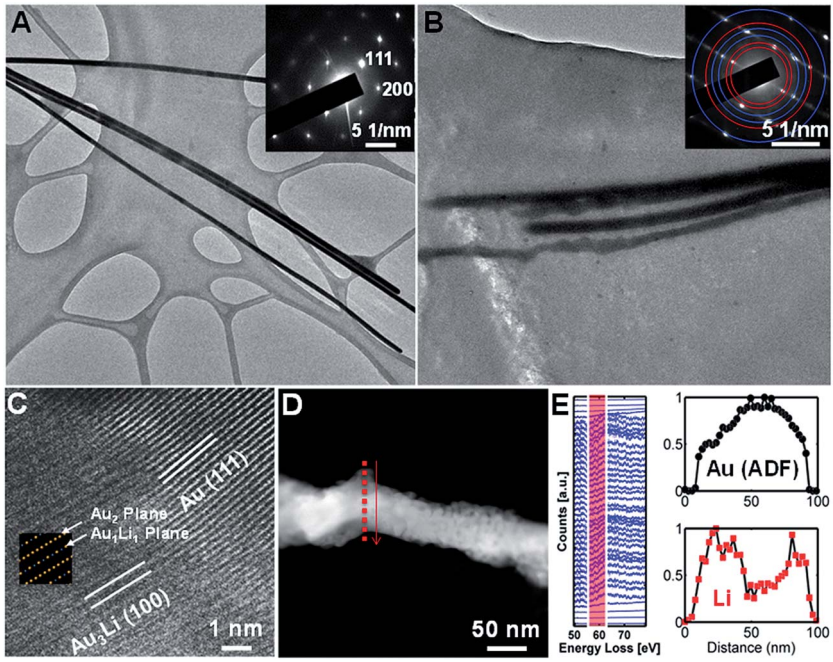

Fig. 9 *Ex situ* TEM studies of gold nanowires before and after the charge cycles. (A) TEM image of gold nanowires before lithiation, and the corresponding selected area electron diffraction pattern (SAED; inset). (B) TEM image of lithiated Au nanowires, and the corresponding SAED (inset). (C) High resolution TEM image of a lithiated Au nanowire with a Au_3Li structure. The alternating planes of Au_2 and Au_1Li_1 are shown in the model structure (Au in yellow; Li in blue). (D) HAADF image of a lithiated Au nanowire. The electron energy loss spectroscopy (EELS) line profile is along the dash line. (E) Extracted lithium and gold concentration along the line profile in (D) with the maximum intensity normalized to 1. The lithium concentration was integrated from the Li K-edge (56–65 eV). (Au O edge contribution in this energy range is negligible. Gold concentration was estimated from the ADF signals.)[23] Reprinted with permission from Z. Y. Zeng, W. I. Liang, H. G. Liao, H. L. L. Xin, Y. H. Chu and H. M. Zheng, *Nano Lett.*, 2014, **14**, 1745–1750. Copyright 2014 American Chemical Society.

study provide some useful information, although intermediate phases are missing.

Conclusions

In this paper, we demonstrated Au lithiation *in situ* by utilizing an electrochemical liquid cell. The observed Li–Au reaction indicated that there are three types of morphology change during Au lithiation: dissolution, explosive reaction and expansion/shrinkage. The possible factors that induce these kinds of Li–Au reactions are discussed. Besides the Li–Au reactions, we also studied bubble formation from electrolyte decomposition and the electron beam effect. The catalytic effects of Au in electrolyte decomposition are observed. More detailed characterization of the intermediate structure during the lithiation of Au is needed by *in situ* study in future work.

Acknowledgements

We used both the MSD TEM facility and TEAM0.5 and CM200 microscopes at the National Center for Electron Microscopy (NCEM) of Lawrence Berkeley National Laboratory (LBNL), which is supported by the U.S. Department of Energy (DOE) under contract # DE-AC02-05CH11231. W.L. is supported by the National Science Council in Taiwan under contract number NSC102-2911-I-009-502. H.Z. thanks the support of the DOE Office of Science Early Career Research Program. We thank Direct Electron, LP (San Diego, CA) for providing the high speed direct electron camera model DE-12 for movie capture.

References

1 W. Xu, J. Wang, F. Ding, X. Chen, E. Nasybulin, Y. Zhang and J.-G. Zhang, *Energy Environ. Sci.*, 2014, **7**, 513–537.
2 M. Gu, Z. Wang, J. G. Connell, D. E. Perea, L. J. Lauhon, F. Gao and C. Wang, *ACS Nano*, 2013, **7**, 6303–6309.
3 J. T. Yin, M. Wada, S. Yoshida, K. Ishihara, S. Tanase and T. Sakai, *J. Electrochem. Soc.*, 2003, **150**, A1129–A1135.
4 Y. J. Lee, Y. Lee, D. Oh, T. Chen, G. Ceder and A. M. Belcher, *Nano Lett.*, 2010, **10**, 2433–2440.
5 H. C. Shin and M. Liu, *Adv. Funct. Mater.*, 2005, **15**, 582–586.
6 W. Luo, S. Lorger, B. Wang, C. Bommier and X. L. Ji, *Chem. Commun.*, 2014, **50**, 5435–5437.
7 Z. Y. Zeng, J. P. Tu, Y. Z. Yang, J. Y. Xiang, X. H. Huang, F. Mao and M. Ma, *Electrochim. Acta*, 2008, **53**, 2724–2728.
8 Z. Y. Zeng, J. P. Tu, X. L. Wang and X. B. Zhao, *J. Electroanal. Chem.*, 2008, **616**, 7–13.
9 Z. Y. Zeng, J. P. Tu, X. H. Huang, X. L. Wang, X. B. Zhao and K. F. Li, *Electrochem. Solid-State Lett.*, 2008, **11**, A105–A107.
10 Z. Y. Zeng, J. P. Tu, X. H. Huang, X. L. Wang and J. Y. Xiang, *Thin Solid Films*, 2009, **517**, 4767–4771.
11 G. Taillades, N. Benjelloun, J. Sarradin and M. Ribes, *Solid State Ionics*, 2002, **152**, 119–124.
12 H. Zheng, R. K. Smith, Y.-w. Jun, C. Kisielowski, U. Dahmen and A. P. Alivisatos, *Science*, 2009, **324**, 1309–1312.
13 H.-G. Liao, L. Cui, S. Whitelam and H. Zheng, *Science*, 2012, **336**, 1011–1014.
14 K. W. Noh and S. J. Dillon, *Scr. Mater.*, 2013, **69**, 658–661.
15 M. Gu, L. R. Parent, B. L. Mehdi, R. R. Unocic, M. T. McDowell, R. L. Sacci, W. Xu, J. G. Connell, P. Xu, P. Abellan, X. Chen, Y. Zhang, D. E. Perea, J. E. Evans, L. J. Lauhon, J.-G. Zhang, J. Liu, N. D. Browning, Y. Cui, I. Arslan and C.-M. Wang, *Nano Lett.*, 2013, **13**, 6106–6112.
16 M. E. Holtz, Y. Yu, D. Gunceler, J. Gao, R. Sundararaman, K. A. Schwarz, T. A. Arias, H. D. Abruña and D. A. Muller, *Nano Lett.*, 2014, **14**, 1453–1459.
17 P. Abellan, B. L. Mehdi, L. R. Parent, M. Gu, C. Park, W. Xu, Y. Zhang, I. Arslan, J.-G. Zhang, C.-M. Wang, J. E. Evans and N. D. Browning, *Nano Lett.*, 2014, **14**, 1293–1299.
18 R. L. Sacci, N. J. Dudney, K. L. More, L. R. Parent, I. Arslan, N. D. Browning and R. R. Unocic, *Chem. Commun.*, 2014, **50**, 2104–2107.

19 C.-M. Wang, X. Li, Z. Wang, W. Xu, J. Liu, F. Gao, L. Kovarik, J.-G. Zhang, J. Howe, D. J. Burton, Z. Liu, X. Xiao, S. Thevuthasan and D. R. Baer, *Nano Lett.*, 2012, **12**, 1624–1632.
20 L. Yuan, H. K. Liu, A. Maaroof, K. Konstantinov, J. Liu and M. Cortie, *J. New Mater. Electrochem. Syst.*, 2007, **10**, 95–99.
21 B. Laik, L. Eude, J. P. Pereira-Ramos, C. S. Cojocaru, D. Pribat and E. Rouviere, *Electrochim. Acta*, 2008, **53**, 5528–5532.
22 P. Bach, A. Seemayer, U. Ruett, O. Gutowski and F. Renner, *DESY Photon Science Annual Reports*, 2012.
23 Z. Y. Zeng, W. I. Liang, H. G. Liao, H. L. L. Xin, Y. H. Chu and H. M. Zheng, *Nano Lett.*, 2014, **14**, 1745–1750.
24 A. D. Pelton, *Bull. Alloy Phase Diagrams*, 1986, **7**, 228–231.
25 P. Limthongkul, Y. I. Jang, N. J. Dudney and Y. M. Chiang, *Acta Mater.*, 2003, **51**, 1103–1113.
26 B. Hvolbæk, T. V. W. Janssens, B. S. Clausen, H. Falsig, C. H. Christensen and J. K. Nørskov, *Nano Today*, 2007, **2**, 14–18.
27 T. V. W. Janssens, A. Carlsson, A. Puig-Molina and B. S. Clausen, *J. Catal.*, 2006, **240**, 108–113.
28 S. H. Overbury, V. Schwartz, D. R. Mullins, W. Yan and S. Dai, *J. Catal.*, 2006, **241**, 56–65.
29 Z. Peng, S. A. Freunberger, Y. Chen and P. G. Bruce, *Science*, 2012, **337**, 563–566.
30 K. Xu, *Chem. Rev.*, 2004, **104**, 4303–4417.
31 M. Sun, H.-G. Liao, K. Niu and H. Zheng, *Sci. Rep.*, 2013, **3**, 3227.
32 H. L. Xin, J. A. Mundy, Z. Y. Liu, R. Cabezas, R. Hovden, L. F. Kourkoutis, J. L. Zhang, N. P. Subramanian, R. Makharia, F. T. Wagner and D. A. Muller, *Nano Lett.*, 2012, **12**, 490–497.